

PAPER

Fractal network dimension and viscoelastic powerlaw behavior: I. A modeling approach based on a coarse-graining procedure combined with shear oscillatory rheometry

To cite this article: Oleg Posnansky *et al* 2012 *Phys. Med. Biol.* **57** 4023

View the [article online](#) for updates and enhancements.

Related content

- [Fractal network dimension and viscoelastic powerlaw behavior: II. An experimental study of structure-mimicking phantoms by magnetic resonance elastography](#)
Jing Guo, Oleg Posnansky, Sebastian Hirsch *et al.*
- [Viscoelasticity-based MR elastography of skeletal muscle](#)
Dieter Klatt, Sebastian Papazoglou, Jürgen Braun *et al.*
- [Multifrequency inversion in magnetic resonance elastography](#)
Sebastian Papazoglou, Sebastian Hirsch, Jürgen Braun *et al.*

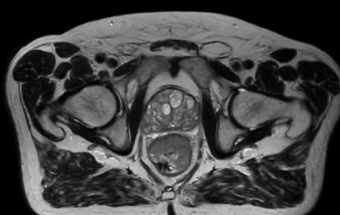
Recent citations

- [Stiffness and Beyond](#)
Ziying Yin *et al*
- [Structural and fractal characterization of adsorption pores of middle-high rank coal reservoirs in western Yunnan and eastern Guizhou: An experimental study of coals from the Panguan syncline and Laochang anticline](#)
Junjian Zhang *et al*
- [Effective diffusion in random composites measured by NMR](#)
Oleg P. Posnansky

Uncompromised.

See clearly during treatment to attack the tumor and protect the patient.

Two worlds, one future.



Captured on Elekta high-field MR-linac during 2018 imaging studies.

 **Elekta**

Elekta MR-linac is pending 510(k) premarket clearance and not available for commercial distribution or sale in the U.S.

Fractal network dimension and viscoelastic powerlaw behavior: I. A modeling approach based on a coarse-graining procedure combined with shear oscillatory rheometry

Oleg Posnansky¹, Jing Guo¹, Sebastian Hirsch¹, Sebastian Papazoglou¹,
Jürgen Braun² and Ingolf Sack^{1,3}

¹ Department of Radiology, Charité-Universitätsmedizin Berlin, Germany

² Institute of Medical Informatics, Charité-Universitätsmedizin Berlin, Germany

E-mail: ingolf.sack@charite.de

Received 1 November 2011, in final form 26 April 2012

Published 7 June 2012

Online at stacks.iop.org/PMB/57/4023

Abstract

Recent advances in dynamic elastography and biorheology have revealed that the complex shear modulus, G^* , of various biological soft tissues obeys a frequency-dependent powerlaw. This viscoelastic powerlaw behavior implies that mechanical properties are communicated in tissue across the continuum of scales from microscopic to macroscopic. For deriving constitutive constants from the dispersion of G^* in a biological tissue, a hierarchical fractal model is introduced that accounts for multiscale networks. Effective-media powerlaw constants are derived by a constitutive law based on cross-linked viscoelastic clusters embedded in a rigid environment. The spatial variation of G^* is considered at each level of hierarchy by an iterative coarse-graining procedure. The establishment of cross-links in this model network is associated with an increasing fractal dimension and an increasing viscoelastic powerlaw exponent. This fundamental relationship between shear modulus dynamics and fractal dimension of the mechanical network in tissue is experimentally reproduced in phantoms by applying shear oscillatory rheometry to layers of tangled paper strips embedded in agarose gel. Both model and experiments demonstrate the sensitivity of G^* to the density of the mechanical network in tissue, corroborating disease-related alterations of the viscoelastic powerlaw exponent in human parenchyma demonstrated by *in vivo* elastography.

³ Author to whom any correspondence should be addressed.

Nomenclature

| | |
|---------------------------------|--|
| $(1), (2)$ | Indices of phase 1 (network) and phase 2 (matrix). |
| $V, V_{(1)}, V_{(2)}$ | Sample volume, volume of phase 1 and volume of phase 2. |
| $\Theta^{(1)}, \Theta^{(2)}$ | Spatial indicators of phases 1 and 2. |
| $\rho(x_k)$ | Binary probability density function for selected k th bond of the lattice. |
| k | Index for a bond in the lattice. |
| $\delta(x)$ | Dirac delta-function. |
| p, q | Concentration (volume fraction) of network and matrix. |
| $R(p)$ | Function of the connectedness of network clusters. |
| p^* | Roots of connectedness function. |
| j | Current number of iteration. |
| ε | Small value chosen as a stopping criterion for iterations. |
| $m_{n,j}, m_j, M$ | Mass of the specific cluster, averaged mass and mass of the fractal. |
| b, l_j, L | Initial scale of the renormalization block, current scale and network size. |
| E, E' | Set of all possible probabilistic configurations of network on a selected renormalization block before and after transformation. |
| Λ | Transformation of configuration space. |
| C_N^n | Binomial coefficients. |
| eff | Index for effective value (stable point of the mapping). |
| ω | Angular frequency of applied external load. |
| τ, t, T | Characteristic relaxation, current time and period of motion. |
| Γ | Boundary of the sample. |
| l, m | Nodes of closest neighbors. |
| α, D_f | Viscoelastic exponent and fractal dimensionality of the network. |
| $\langle \dots \rangle$ | Statistical averaging over different configurations. |
| \vec{f} | External tangential force applied to the sample surface. |
| η, μ | Shear viscosity and shear modulus. |
| K, ξ | Volumetric modulus and volumetric viscosity. |
| $\sigma_{qs}, \varepsilon_{qs}$ | Tensors of stress and strain. |
| G^*, G', G'' | Complex-valued shear modulus, storage modulus and loss modulus. |

Introduction

Medical imaging in combination with mechanical tissue stimulation has evolved into a new class of diagnostic tools subsumed under the term elastography. Today, elastography either based on medical ultrasound (Parker *et al* 1990, Ophir *et al* 1991) or magnetic resonance imaging (Muthupillai and Ehman 1996, Plewes *et al* 1995) is increasingly applied for the clinical assessment of a variety of diseases from liver fibrosis (Ziol *et al* 2005, Yin *et al* 2007) to breast cancer (Xu *et al* 2010, Sinkus *et al* 2007). Initially focused on the measurement of the shear elasticity of tissue, recent advances in elastography have addressed the dynamics of the shear modulus, which represents the shear viscoelastic properties of a material within the examined dynamic range (Vappou *et al* 2007, Klatt *et al* 2007, Zhang *et al* 2008, Hoyt *et al* 2008, Deffieux *et al* 2009, Gennisson *et al* 2010, Riek *et al* 2011, Clayton *et al* 2011). In general, the linear shear viscoelasticity is quantified by the complex-valued shear modulus G^* with a real part G' that is related to the restoration of mechanical energy (referred to as a storage modulus) and the imaginary part G'' related to the lossy behavior of a material (termed as loss modulus). G^* displays scaling in materials composed of complex hierarchical networks, i.e. the viscoelastic information of microsubsets of network elements is conveyed

through all scales of network hierarchy up to effective, i.e. global, constants (Gurtovenko and Blumen 2005, Magin and Royston 2010). For this reason, dynamic elastography is sensitive to the pathological alteration of tissue on a scale far below image resolution.

To date, the dynamics of G^* measured by elastography is usually quantified by parameters which are related to the combination of basic spring and dashpot elements (Klatt *et al* 2007). Classical viscoelastic models such as the Voigt or Maxwell model cannot provide direct insight into the underlying network structure as they refer to homogeneous materials. Conversely, multiscale networks have a structure resulting in heterogeneity on all scales (Jeong *et al* 2000). Fundamental conclusions about the hierarchy of mechanical networks can be drawn by considering a viscoelastic powerlaw, $G^* \sim (i\omega)^\alpha$, where α is the powerlaw exponent and ω is the angular drive frequency. Such a powerlaw implies that the spatial variation of G^* at a microlevel is incorporated into the viscoelastic properties of a single element of higher hierarchy. It has been observed in elastography and biorheology that the dynamics of G^* in various biological tissues obeys a powerlaw with $\alpha < 1/2$ (Geerligs *et al* 2008, Klatt *et al* 2010a, Zhang *et al* 2008, Riek *et al* 2011). Such powerlaw behavior can be interpreted by linear alignment of viscous beds interconnected by springs. This so-called Rouse chain has $\alpha = 1/2$; however, the relevant range of $\alpha < 1/2$ in a biological tissue can be modeled by considering the spring constants as being hierarchically ordered by the number of vibration modes (Schuessel and Blumen 1995). However, this model introduces an additional hierarchy of elastic constants, making α dependent on both structure and rigidity and thus rendering the interpretation of α solely by structure-related parameters rather cumbersome.

We therefore propose a theoretical framework of multiscale averaging and effective-medium theory for describing the powerlaw dynamics in a biological tissue. The key point of this theoretical framework is based on a coarse graining of physical properties of heterogeneous materials starting on the minimal characteristic scale and ending at a size where heterogeneity is no longer distinguishable. This theory was originally developed to describe effective transport in disordered media (Milton 2002, Schuessel and Blumen 1995). Adopting this method for elastography, we assume that the network topology is dictated by the randomness and statistical self-similarity of structures throughout all scales. Viscoelastic properties of mechanical networks are then derived by the theory of critical phenomena and phase transitions (Stanley 1978, Domb and Lebowitz 2001, Landau *et al* 1980). The fractal dimension of the self-similar network is used as a parameter related to the density of the network. In this way, we aim to simulate the relationship between the viscoelastic powerlaw exponent and the number of multiscale cross-links in a biological tissue. We further seek to validate principal findings by experiments of shear oscillatory rheometry of agarose layers with and without an embedded network structure. The two-dimensional (2D) network made from thin tangled paper strips embedded in the gel matrix was inspired by the random network created during simulations. Conversely, as a starting point of the simulations, a pure elastic matrix was taken into account similar to what we observed in rheometer experiments of plain and low-concentration agarose. Therewith, we linked simulations and experiments for studying the powerlaw properties of the complex modulus of soft tissue in the dynamic range relevant for *in vivo* elastography.

Theory

A hierarchical probabilistic tissue model

In the following we will regard tissue as a two-phase random structure possessing a self-similar geometry across all scales (figure 1(a)). The material occupies region $V \in R^d$, where d is the topological dimension of the Euclidean space. V is partitioned into two disjoint random

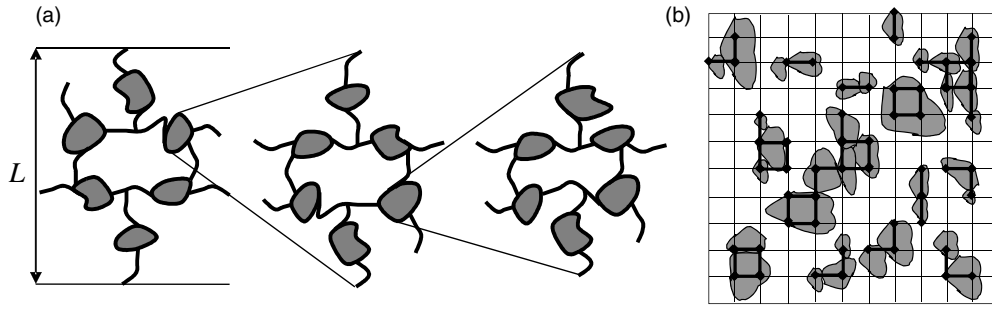


Figure 1. (a) Biological tissue is represented as a network of cell membranes of size L with hierarchical properties. The right-hand side of the diagram emphasizes the self-similar structure of the network. (b) Mapping of tissue on a lattice. The bold bonds describe properties of the membrane, while thin bonds belong to the extracellular space. Mapping rules include variations in size, shape and volume fraction of the complex structure of the biological tissue.

sets: phase 1 of region $V_{(1)}$ and volume $V_{(1)}$ and phase 2 of region $V_{(2)}$ and volume $V_{(2)}$. We map the occupied region V on a square lattice (figure 1(b)) and consider a finite and countable set of all realizations, $E \in \Omega$ of sample space Ω of phases 1 and 2 (Feller 1968). The mapping rules include variations in size, shape and volume fraction of the composite structure. Spatial inhomogeneities are represented by the lattice junctions, and the interjunction bonds simulate mechanical adhesion of neighbors. For N lattice bonds and n bonds of phase 1, we find $\sum_{n=0}^N C_N^n = 2^N$ realizations (or configurations) partitioned on binomial coefficients C_N^n . Binomial coefficients determine the number of configurations with fixed n bonds of phase 1 and define the upper limit of the number of connectedness of the lattice. Every bond in the lattice can either belong to phase 1 or phase 2 with a probability of $p \in [0, 1]$ or $q = 1 - p$, respectively. The probability of the n th partitioning is equal to $p^n q^{N-n}$ according to the rules of probabilistic binomial logic. For a given realization E of the two-phase random medium, the indicator function $\Theta_k^{(l)}$ for phase $l = \{1, 2\}$ is defined as

$$\Theta_k^{(l)} = \begin{cases} 1, & \vec{r}_k \in V_{(l)}(E) \\ 0, & \vec{r}_k \notin V_{(l)}(E) \end{cases} \quad (1)$$

with

$$\Theta_k^{(1)} + \Theta_k^{(2)} = 1, \quad (2)$$

where the indices run with $k = \overline{1, N}$, numbering bonds in the lattice. \vec{r}_k is a radius vector pointing to the k th bond. If the concentration of phase 1 is fixed, p and q are given as

$$p = V_{(1)} / (V_{(1)} + V_{(2)}) \text{ and } q = V_{(2)} / (V_{(1)} + V_{(2)}), \quad (3)$$

with $V_{(1,2)} / (V_{(1)} + V_{(2)}) = \langle \Theta_k^{(1,2)} \rangle$. Note that the local weighted average of any realization of an arbitrary function $\phi(\Theta_k^{(1,2)})$ is

$$\langle \phi(\Theta_k^{(1,2)}) \rangle = p \phi(\Theta_k^{(1)}) + q \phi(\Theta_k^{(2)}), \quad (4)$$

where Θ emphasizes the binary distribution of function ϕ . Combining discrete and continuous distributions of any physical parameter x_k for the k th bond, it is possible to introduce a generalized binary local probability density function $\rho(x_k)$ using Dirac delta function $\delta(x)$ and equation (4):

$$\rho(x_k) = p \delta(x_k - y^{(1)}) + q \delta(x_k - y^{(2)}). \quad (5)$$

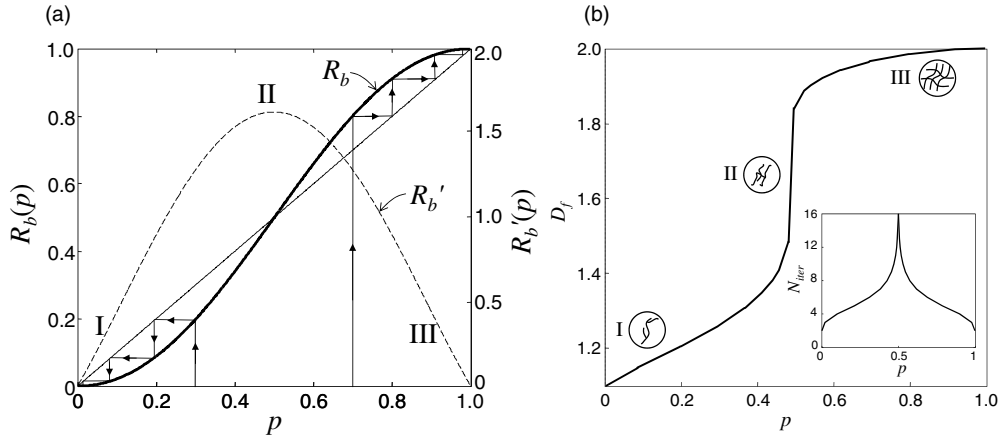


Figure 2. (a) Connectedness function $R_b(p)$ (bold solid line) and its derivative $R'_b(p)$ (dashed line). The physically meaningful roots (solutions) or fixed points of the recursive equation (6) are $p_* = \{0, 0.5, 1\}$. Point $p_* = 0.5$ belongs to unstable region II. Any disturbance of p within region II leads to a stable zone I or III with fixed points $p_* = 0$ or $p_* = 1$. Zigzag pathways represent examples of evolution of p during execution of equation (7) starting at $p = 0.3$ and $p = 0.7$. (b) Fractal dimension D_f as a function of network volume fraction p . In region I the network resembles isolated chains with $D_f \sim 1$ (D_f might be slightly above 1 due to short branches on the chains). In region II clustering effects become increasingly relevant, yielding region III, which evolves into an ideal network with translational symmetry and $D_f \sim 2$. The pictograms inside the circles illustrate the transformation of the network topology. The number of iterations, N_{iter} (maximum limit of iteration index j), performed during execution of equation (7), is shown in the inset. In the limit cases $p = 0$ or $p = 1$, only two iterative steps are needed: one for assigning properties of every bond and a second for averaging. The number of iterations increases near $p = 0.5$ with a maximum number of lattice bonds of 8^{16} .

In equation (5), $y^{(1,2)}$ is a fixed physical parameter for the binomial distribution. The challenge is to model effective parameters of a material with randomly distributed local properties according to equation (5). A very practical real space renormalization group for the calculation of the structural properties of a random lattice was introduced by Reynolds *et al* (1977). In the appendix this method is described in a generalized way.

The basic idea of this method is to group bonds on subregions of size b by accounting for all possible bond distributions within the random lattice. This procedure prescribes a transformation R_b depending on the probability p of the network (phase 1) and the probability $(1 - p)$ of the matrix (phase 2):

$$R_b(p) = p^5 + 5p^4(1 - p) + 8p^3(1 - p)^2 + 2p^2(1 - p)^3. \quad (6)$$

After transformation R_b , a coarse-grained version of the lattice is obtained where every bond has a new probability equal to $R_b(p)$ if it belongs to the composite network. This transformation can be repeated according to the recursive relation

$$p_{j+1} = R_b(p_j) \quad (7)$$

for iteratively building a self-similar structure with an increasing level of hierarchy j . The function $R_b(p)$, along with its derivative, is plotted in figure 2(a). Zigzag pathways represent evolution of p_j during execution of equation (7). The number of iterations for building a hierarchical lattice is defined by the constraint $|p_j - p_{j+1}| \leq \varepsilon$ with $\varepsilon = 10^{-3}$. Due to this condition, the two phases are indistinguishable after multiscale hierarchical averaging.

The fractal dimension of the network

We calculate fractal dimensionality D_f for the network according to its effective mass M and extension L by Mandelbrot (1983):

$$D_f = \log_{10}(M) / \log_{10}(L). \quad (8)$$

M is given as

$$M = \lim_{j \rightarrow \infty} (m_j) \quad (9)$$

with the mass m_j of the network cluster at a single recursion level j ,

$$m_{j+1} = \sum_n m_{n,j} p_j^n q_j^{N-n}, \quad (10)$$

which is the sum of the mass of different configurations n ; N is the number of all bonds in the lattice of renormalization. The effective, i.e. global, size L of the network is defined by the size of each block of bonds l and the number of hierarchical levels:

$$L = \lim_{j \rightarrow \infty} (l_j) = b^j. \quad (11)$$

In figure 2(b) the fractal dimension D_f is presented as a function of the concentration of the network calculated according to equations (8)–(11) and assuming unity mass of bond at the first recursion level ($m_{1,1} = 1$). At very low concentrations, the occupied bonds in the lattice assemble to form chain-like structures, resulting in fractal dimensionality $D_f \sim 1$. D_f of the network at low p might be slightly above 1 due to short branches in the effective chain. When network concentration p increases, an increasing amount of branches and inter-chain cross-links appears, creating an ideal mesh at $p = 1$ with $D_f = 2$. The most significant change in fractal dimensionality is seen near $p = 0.5$. There, the change from chain to cluster topology appears as a kind of phase transition. The number of multiscale averages N_{iter} is correlated with the degree of heterogeneity within the network. At both limits, $p \rightarrow 0$ and $p \rightarrow 1$, only two iterative steps are needed: the first is to assign the properties of each bond, while in a second step, the physical or geometrical property is averaged. The number of averages largely increases in the vicinity of $p = 0.5$, which corresponds to the maximum of heterogeneity. At this point, the size of the lattice approaches 2^{16} of relative units (see the inset of figure 2(b)). The relationship between fractal dimension and effective viscoelastic properties is analyzed in the next section.

Viscoelastic properties of the network

Both viscous and elastic components contribute to the global response of a biological tissue. In our biphasic model, both contributors are microscopically separated and assigned to matrix and bonds. Let τ be a characteristic time during which internal stresses are completely relaxed. Suppose that tissue is under periodically applied tangential external shear load $\vec{f}|_{\Gamma} = \vec{f}_0 e^{-i\omega t}$, where Γ is a boundary of the sample. If the period of motion $T \sim 1/\omega$ is large compared to relaxation time τ ($\omega\tau \ll 1$), then tissue at the microlevel behaves as an element with dominant damping and such a regime is termed quasi-static. In contrast, when frequency ω is large and $\omega\tau \gg 1$, the tissue at microlevel possesses mainly elastic properties. Consequently, two basic coefficients, shear viscosity η and shear modulus μ , are introduced to describe the intermediate state, i.e. the viscoelastic material behavior. For the elastic case, the relationship between the tensors of stress σ_{qs} and strain ε_{qs} is given by Hooke's law (Landau *et al* 1980):

$$\sigma_{\text{qs}} = K \varepsilon_{\text{II}} \delta_{\text{qs}} + 2\mu \left(\varepsilon_{\text{qs}} - \frac{1}{3} \delta_{\text{qs}} \varepsilon_{\text{II}} \right), \quad (12)$$

which is given here in Cartesian component notation and implying summation over repeating indices. K denotes the bulk modulus and δ_{qs} is a Kronecker symbol. For the pure viscous case, we correspondingly find

$$\sigma_{qs} = \xi \dot{\varepsilon}_{ll} \delta_{qs} + 2\eta \left(\dot{\varepsilon}_{qs} - \frac{1}{3} \delta_{qs} \dot{\varepsilon}_{ll} \right), \quad (13)$$

where ξ and η are volume and shear viscosities. Assuming that the biological tissue is incompressible and mediates only transverse waves, we restrict our attention to the tensor components $q \neq s$. In the limit of a pure elastic body, Hooke's law (equation (12)) can then be simplified to

$$\sigma_{qs} = \mu \varepsilon_{qs}, \quad (14)$$

and equation (13) to

$$\sigma_{qs} = \eta \dot{\varepsilon}_{qs}, \quad (15)$$

which is in the frequency domain

$$\sigma_{qs} = -i\eta\omega\varepsilon_{qs} \quad (16)$$

if we take into account engineer notations for strains cancelling out the factor 2 in equation (13).

Equations (14) and (16) can be combined to a general form of Hooke's law

$$\sigma_{qs} = G^*(\omega, \vec{r}) \varepsilon_{qs}, \quad (17)$$

by introducing the complex-valued shear modulus G^* , whose real and imaginary parts are related to storage modulus and loss modulus, respectively:

$$G^*(\omega, \vec{r}) = G'(\omega, \vec{r}) + iG''(\omega, \vec{r}). \quad (18)$$

Classical viscoelastic models such as the Maxwell or Voigt model can be considered for defining G^* by viscoelastic constants μ and η . For example, if we assume that the Voigt model is valid within the local area specified by \vec{r} , the complex shear modulus is given according to equations (14) and (16) with

$$G^*(\omega, \vec{r}) = \mu(\vec{r}) + i\omega\eta(\vec{r}). \quad (19)$$

In equation (17) the solution of an elastic problem is treated as the solution of a viscoelastic problem by transforming real-valued elastic modulus μ to complex-valued G^* . Such a transition is often termed as the principle of correspondence and in general, the problem can be considered as quasi-static (Carcione 2007).

The balance of all forces in the vicinity of location \vec{r} and in the absence of external body forces assumes a conservation law

$$\frac{\partial}{\partial x_s} (G^*(\omega, \vec{r}) \varepsilon_{qs}) = 0. \quad (20)$$

In our model, we assume the matrix (phase 2) to be dominated by elastic properties, i.e. $G' \gg G''$, while G'' tends to increase with the establishment of network connections. This assumption is motivated by observations made in agarose gel, which is a nearly perfect elastic matrix for embedding fiber structures. In the experiments presented later, the fibers are made from thin paper strips causing a significant increase in lossy properties of the effective medium. We therefore introduce here into our model a large dissipative term for the network ($G''(\omega, \vec{r}) \sim G'(\omega, \vec{r})$).

Equation (20) can be written in a finite-difference form (Barbero 2007)

$$\sum_k^N G_k^*(\omega) (u_l - u_m) = 0, \quad (21)$$

if displacement in the direction parallel to the external force dominates and strain is approximated by $\varepsilon_{qs} \approx (u_q(l) - u_q(m)) / \Delta x_s$. In equation (21) we factor out and exclude a lattice constant $a = \Delta x_s$. Indices in brackets (lm) denote the closest neighbor nodes which determine the edges of the corresponding bond k . Solving equation (21) numerically combined with the Dirichlet (or first-type) boundary condition, we can estimate the *monoscale effective* complex-valued shear modulus as

$$G^{*,\text{eff}} = \left\langle \int_{\vec{r} \in V} \sigma_{qs}(\vec{r}) d\vec{r} \right\rangle_E \bigg/ \left\langle \int_{\vec{r} \in V} \varepsilon_{qs}(\vec{r}) d\vec{r} \right\rangle_E, \quad (22)$$

where the local distribution of G_k^* is specified according to equation (5) with $x = G_k^*$. In equation (22) averaging is applied twice: the first average $\int (\dots)$ is applied over the whole sample volume V while the second average $\langle \dots \rangle$ is the weighted ensemble average E over different configurations. In the context of the previously introduced iterative averaging scheme, the complex shear modulus depends on scale number j . At the lowest scale level $j = 1$, every bond in the lattice can possess either pure elastic properties (e.g., considering the gel matrix) or prevalent damping properties (due to the embedded network). Thus the probability density function of G^* at the lowest scale level $j = 1$ on the k th bond takes the form

$$\rho_1(G_k^*) = p_1 \delta(G_k^* - G_1^{(1)}) + q_1 \delta(G_k^* - G_1^{(2)}), \quad (23)$$

where subscript indices denote j and the superscripts refer to phase 1 (matrix) or phase 2 (solid network). Equation (23) fully determines the local properties in the distribution of G^* . On the scale level $j = 2$ the function is

$$\rho_2(G_k^*) = p_2 \delta(G_k^* - G_2^{(1)}) + q_2 \delta(G_k^* - G_2^{(2)}) \quad (24a)$$

or equivalently

$$\begin{aligned} \rho_2(G_k^*) &= \int_{E=\{G_{1,\dots,N}^*, \rho_1\}} dG_1^* dG_2^* \dots dG_n^* \dots dG_N^* \rho_1(G_1^*) \\ &\dots \rho_1(G_2^*) \dots \rho_1(G_N^*) \delta(G_k^* - G_2^{(1,2)}). \end{aligned} \quad (24b)$$

The superscript index in $G_2^{(1,2)}$ is chosen depending on connectedness of the network: $G_2^{(1)}$ determines network embedded in the matrix and $G_2^{(2)}$ characterizes the matrix with fragmented network elements (we use only one symbol, ρ , for both cases because on a lattice with probabilistic bonds, we can find a connected or fragmented network), and

$$G_2^{(1,2)} = \left\langle \int_{\vec{r} \in V} d\vec{r} \sigma_{qs}(\vec{r}) \right\rangle_{E=\{G_{1,\dots,N}^*, \rho_1\}} \bigg/ \left\langle \int_{\vec{r} \in V} d\vec{r} \varepsilon_{qs}(\vec{r}) \right\rangle_{E=\{G_{1,\dots,N}^*, \rho_1\}}, \quad (25)$$

where the averaged shear moduli $G_2^{(1)}$ and $G_2^{(2)}$ characterize either the connected effective network or the matrix. In general, equations (24a) and (25) can be written as

$$\rho_j(G_k^*) = p_j \delta(G_k^* - G_j^{(1)}) + q_j \delta(G_k^* - G_j^{(2)}) \quad (26a)$$

or

$$\rho_j(G_k^*) = \int_{E=\{G_{1,\dots,N}^*, \rho_{j-1}\}} \left(\prod_{n=1}^N dG_n^* \rho_{j-1}(G_n^*) \right) \delta(G_k^* - G_j^{(1,2)}) \quad (26b)$$

and

$$G_j^{(1,2)} = \left\langle \int_{\vec{r} \in V} d\vec{r} \sigma_{qs}(\vec{r}) \right\rangle_{E=\{G_{1,\dots,N}^*, \rho_{j-1}\}} \bigg/ \left\langle \int_{\vec{r} \in V} d\vec{r} \varepsilon_{qs}(\vec{r}) \right\rangle_{E=\{G_{1,\dots,N}^*, \rho_{j-1}\}}. \quad (27)$$

Table 1. List of input numerical parameters used in the simulations of viscoelastic dynamic properties of a matrix-embedded network. The mechanical properties were chosen to satisfy a quasi-static limit.

| Input parameter | Value |
|-----------------------------------|-------------|
| p , network | [0;1] |
| $\omega/2\pi$ | [20;100] Hz |
| $\text{Re}(G^*)$, matrix | 0.01 Pa |
| $\text{Im}(G^*)$, matrix | 0 Pa |
| $\text{Re}(G^*)$, network | 0.01 Pa |
| $\text{Im}(G^*)/\omega$, network | 0.01 Pa s |

The scale averaging procedure is repeated with the increasing level j as long as $|p_j - p_{j+1}| \leq \varepsilon$ with $\varepsilon = 10^{-3}$ is fulfilled. If this procedure converges, the probability density function becomes singular:

$$\rho_j(G_k^*)|_{j \rightarrow \infty} = \delta(G_k^* - G_j^{(1,2)}). \quad (28)$$

We term the value $G_j^{(1)}|_{p>0.5; j \rightarrow \infty} = G^{*,\text{eff}}$ or $G_j^{(2)}|_{p<0.5; j \rightarrow \infty} = G^{*,\text{eff}}$ a *multiscale effective* shear modulus, emphasizing its iterative self-similar nature. $G^{*,\text{eff}}$ can be approached from two sides of concentration of the network if $G_j^{(1)}|_{p_+=0.5, j \rightarrow \infty} = G_j^{(2)}|_{p_-=0.5, j \rightarrow \infty} = G^{*,\text{eff}}$. Summarizing the described procedure, we write a closed sequence of parameters on scales $j+1$ based on the initial state $j = 1$ given in equation (23) and the quasi-static balance of all local forces as denoted in equations (20) and (21):

$$\begin{cases} p_{j+1} = R_b(p_j) \\ G_{j+1}^{(1,2)} = \left\langle \int_{\vec{r} \in V} d\vec{r} \sigma_{\text{qs}}(\vec{r}) \right\rangle_{E=\{G_{1,\dots,N}^*, \rho_j\}} \bigg/ \left\langle \int_{\vec{r} \in V} d\vec{r} \varepsilon_{\text{qs}}(\vec{r}) \right\rangle_{E=\{G_{1,\dots,N}^*, \rho_j\}} \\ \rho_{j+1}(G_k^*) = \int_{E=\{G_{1,\dots,N}^*, \rho_j\}} \left(\prod_{n=1}^N dG_n^* \rho_j(G_n^*) \right) \delta(G_k^* - G_{j+1}^{(1,2)}) \end{cases} \quad (29)$$

The external shear load of frequency ω is included in the boundary condition of equation (29). The solution of equation (29) provides a fixed point dependent on the initial concentration of the network. It determines the multiscale effective properties of the tissue.

Methods

Numerical simulations

Equation (29) was numerically solved using Matlab© 7.5 (The Mathworks Inc. Natick, MA) run on a 2.83 GHz personal computer equipped with 8 GB working memory. Computation time for a simulation comprising 16 recursion steps was in the order of 3.9 s. Initial parameters are listed in table 1. Shear storage and loss properties of the network were considered to be comparable and consequently the real and imaginary parts of $G_1^{(1)}$ were in a similar range. Based on our observations in agarose, the matrix modulus $G_1^{(2)}$ was chosen with negligible dissipation, yielding no dispersion over frequency.

Phantom preparation and shear oscillatory rheometry

To produce thin gel matrix layers for shear oscillatory rheometry, an agar–water solution (Fluka, BioChemika) of 0.5 mass% was cast into a cylindrical cavity of 3 cm radius and

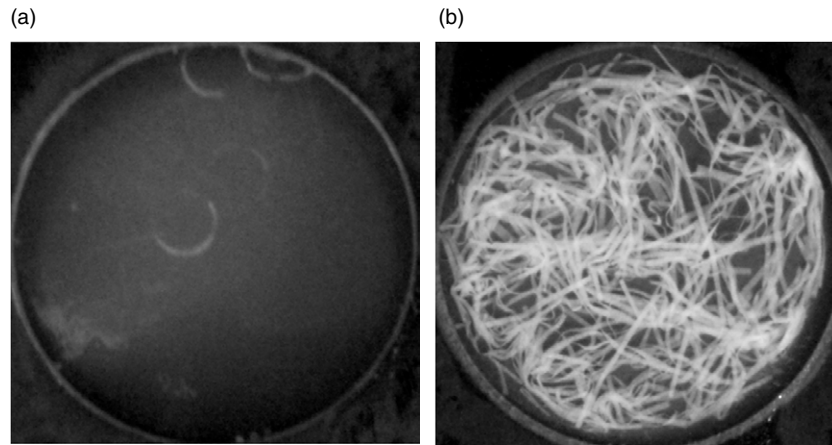


Figure 3. Top views of the experimentally investigated samples. (a) Plain agar gel. (b) Agar gel with paper strips mimicking random structure with cross-links due to inter-chain friction.

2 mm depth lathed in a plastic plate. Two phantoms were built: one plain gel phantom as a reference for matrix viscoelastic properties and a second one consisting of thin paper strips embedded in a gel matrix. The paper strips of 70 mm length and 1 mm thickness were cut from a cigarette paper (OCB, R J Reynolds Tobacco Company, Winston-Salem, NC, USA) of size $7 \times 4 \text{ cm}^2$ and mass $7 \times 10^{-2} \text{ g}$. Prior to adding the agarose solution, the tangled paper was pressed to a flat disk and placed within the chilling mold so that no strip exceeded the rim of the cavity (figure 3). The fractal dimension of the network was estimated by the box-counting method (Mandelbrot 1983), resulting in $D_f = 1.72$. After solidification, the gel layers were consecutively investigated *in situ* by placing the whole chill mold beneath the circular transducer plate ($\varnothing 50 \text{ mm}$) of the rheometer (MCR 301, Anton Paar, Austria). The shear storage and loss moduli were monitored in the linear regime of 0.2% strain amplitude and in a frequency range between 20 and 65 Hz. Previous studies reported consistent modulus values up to 62.5 Hz in bovine liver samples (Klatt *et al* 2010a) and up to 100 Hz in agarose (Papazoglou *et al* 2012) based on the same rheometer device and shearing plate as used herein. Causality of G^* -data measured by our device in plain agarose was addressed in Papazoglou *et al* (2012) exploiting the Kramers–Kronig relationship between the real and imaginary parts of G^* . All experiments were repeated three times for testing the variability of the method.

Results

Figure 4(a) portrays the evolution of the binary local probability density function, $\rho_j(|G^{*,\text{eff}}|)$. The initial values for network concentration and matrix fraction were $p_1 = 0.6$ and $q_1 = 0.4$, respectively. The excitation frequency was $\omega/(2\pi) = 60 \text{ Hz}$. To emphasize the trend of evolution of $\rho_j(|G^{*,\text{eff}}|)$, the envelopes of weights of δ functions are drawn. The heights of these functions are equal to weights p_j and q_j , while their positions are determined by the magnitude of shear modulus $|G^{*,\text{eff}}|$. Arrows indicate the variation of $|G^{*,\text{eff}}|$ in the parameter space. It is well visible that an increasing number of iterations leads to the degeneration of the binary function to singularity, i.e. scale averaging reduces the matrix fraction towards zero ($q_j|_{j \rightarrow \infty} \rightarrow 0$), while the network fraction increases and approaches unity ($p_j|_{j \rightarrow \infty} \rightarrow 1$). At this scale, the sample is completely occupied by bonds with effective properties $|G^{*,\text{eff}}|$.

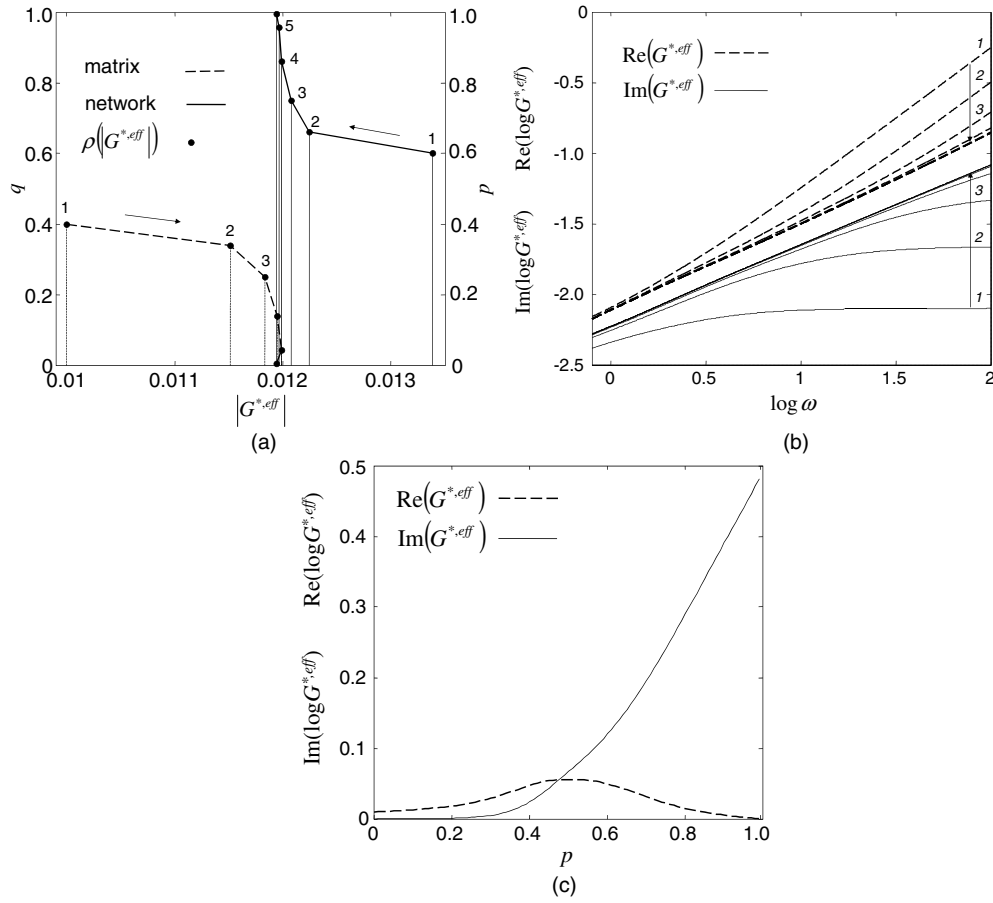


Figure 4. (a) Evolution of the local matrix network probability density function $\rho(|G^*|)$ during multiscale averaging. The initial values for network and matrix fractions were $p = 0.6$ and $q = 0.4$, respectively, and the drive frequency was $\omega/2\pi = 60$ Hz. Envelopes of weights of the δ functions are drawn for illustrating the trend of the evolution of the probability density function. Arrows indicate the movement of $\rho(|G^*|)$ in parameter space $(p; q; |G^*|)$. The numbers given in the plot are the steps of iterations for both phases. (b) Evolution of dispersion curves of real and imaginary parts of complex-valued shear modulus $G^*(\omega)$ at the network concentration $p = 0.54$. The dispersion curves calculated by multiscale averages from 1 to 3 are correspondingly labeled. Powerlaw dynamics is approached by further increasing the evolution numbers as indicated by arrows. (c) Dependence of real and imaginary parts of complex-valued shear modulus $G^{*,\text{eff}}(\omega, p)$ as a function of network concentration p . In the region $p < 0.5$, the real part of $G^{*,\text{eff}}(\omega, p)$ is dominating and for $p > 0.5$ the imaginary part of $G^{*,\text{eff}}(\omega, p)$ is dominating.

determined solely by the network and different from the initial input. Such effective properties are characterized by the mixed properties of both matrix and network. In figure 4(a) it is stressed that the probability density function comprises two delta functions according to equation (5). Thus, at the first iteration step $j = 1$, ρ either represents matrix or network properties. With $j > 1$, the effective bond is assembled from lower scale networks comprising elements of the matrix. At the same time, the matrix comprises fragmented elements of disconnected network. The coarse-graining procedure digitizes our system to a binary geometry of 0 and 1 as reflected by the singular character of the probability density function at points of convergence.

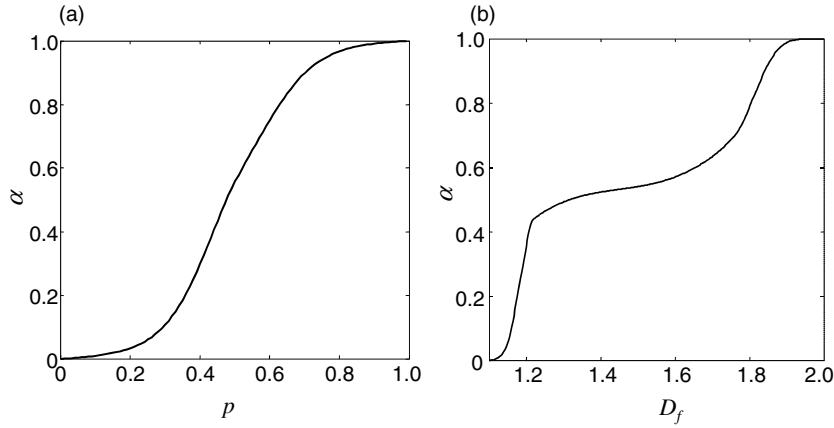


Figure 5. The powerlaw coefficient α as a function of network concentration p (a) and fractal dimension D_f (b).

We further investigate the behavior of the system as a function of angular drive frequency ω . Various dispersion curves of both real and imaginary parts of $G^*(\omega)$ at network concentration $p = 0.54$ are presented in figure 4(b). An increasing number of multiscale averages j leads to linearization of the dispersion curves in the double logarithmic plot, i.e. the behavior of $G^*(\omega)$ is increasingly well represented by a powerlaw. Since the multiscale network is self-similarly linked, an increasing geometrical complexity bears relatively simple analytics. At certain evolution numbers, the effective shear modulus exhibits a distinct powerlaw such as

$$G^{*,\text{eff}}(\omega, p) \sim \omega^{\alpha(p)} f(G_1^{(1,2)}, p), \quad (30)$$

with the powerlaw coefficient α and the complex-valued function $f(G_1^{(1,2)}, p)$, which depends on the ratio between storage and loss components of effective shear modulus and the network concentration. In figure 4(c) the real and imaginary parts of complex-valued shear modulus $G^{*,\text{eff}}(\omega)$ are shown as functions of network concentration p . In the region $p < 0.5$, the real part of $G^{*,\text{eff}}(\omega)$ is dominating and in $p > 0.5$ the imaginary part of $G^{*,\text{eff}}(\omega)$ is dominating. The real and imaginary parts of the complex-valued shear modulus coincide with each other in the vicinity of the unstable point $p = 0.5$ (one of the roots of equation (7)).

Since a powerlaw in G^* implies a constant ratio of $G'' = \text{Im}(G^*)$ and $G' = \text{Re}(G^*)$, we can derive α by Klatt *et al* (2010b)

$$\alpha(p) = \frac{2}{\pi} \arctan\left(\frac{G''}{G'}\right). \quad (31)$$

α is determined by the viscoelastic properties of the dominating phase, depending on whether the system is below or above $p = 0.5$. Figure 5(a) presents α as a function of network concentration p . Similar to $D_f(p)$ shown in figure 2(b), α is determined by the viscoelastic properties of the matrix for $p < 0.5$ and of the network for $p > 0.5$. However, the change in α with p occurs at different rates compared to D_f . Plotting α versus fractal dimension D_f (figure 5(b)) indicates the sensitivity of α to the density of random network connections. Apparently, $\alpha(D_f)$ is a nonlinear function which displays a plateau-like behavior from $D_f \sim 1.3$ to 1.6 and two regimes of high sensitivity. Low α values (< 0.4), as encountered in a soft biological tissue (Klatt *et al* 2010b), correspond to the region of high sensitivity, i.e. a moderate variation in D_f of about 1% would alter α by about 6%. Figure 6 shows the

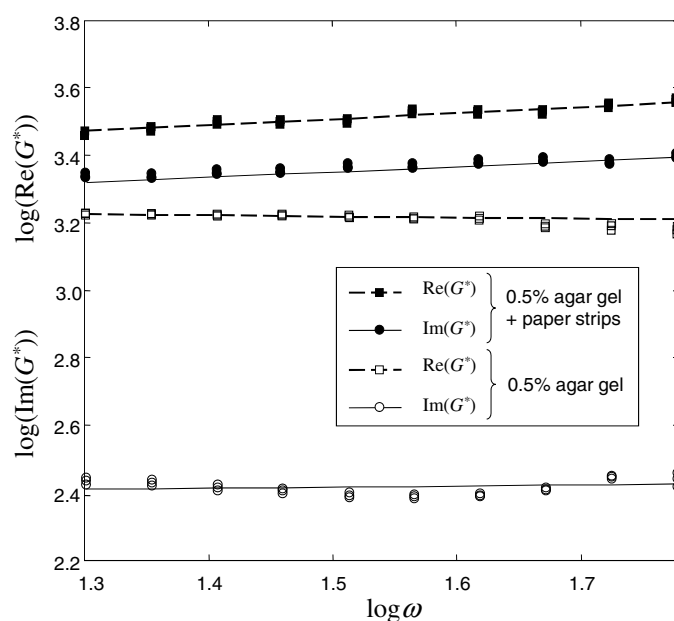


Figure 6. Dispersion functions for agar gel with and without paper strips building a random structure. The experimental data represented by symbols were fitted by linear regression (line graphs), yielding a slope α equal to 0.310 ± 0.006 and 0.080 ± 0.015 for agar gel with and without structure, respectively. Experiments were repeated three times to assess the variability of the method.

experimentally measured dispersion of storage and loss moduli of a plain agar sample and a phantom containing tangled paper strips embedded in a gel matrix. The fractal dimension of the sample with added paper strips was 1.72. Both samples show a powerlaw behavior within the examined frequency range. The slight decrease of G' in plain agarose in the higher dynamic range is considered an artifact most likely due to slip between sample and rheometer plate at higher oscillation frequencies. The order of both G' and G'' measured in plain gel is in good agreement to data in the literature (Papazoglou *et al* 2012). Without paper strips, agarose presents with small values of $\alpha = 0.08 \pm 0.015$, whereas adding random paper networks increases α to 0.310 ± 0.006 , according to equation (31). In addition to changing α , the paper strips also influence the elasticity of the sample related to $G' = \text{Re}(G^*)$. However, the paper-induced increase in G' by about a factor of 1.7 is much less pronounced than the increase of $G'' = \text{Im}(G^*)$ by about a factor of 6.4. Therewith, the ratio of G''/G' changes by about a factor of 4.1, which is 2.5 times higher than the alteration of the storage modulus, indicating the high sensitivity of α to the structure added to the gel matrix.

Discussion and conclusion

A multiparametric recursive procedure was introduced for simulating the viscoelastic properties of self-similar random networks. Self-similar random geometries resemble multiscale networks of many soft biological tissues and provide a numerically efficient way to model the relationship between microscopic and macroscopic physical properties. In this study, we focused on the powerlaw behavior of the shear modulus G^* of an effective medium

composed of viscoelastic chains embedded in a purely elastic matrix. This model differs from approaches in polymer physics where viscoelastic polymer chains are considered to be suspended in a viscous environment. As a result of our model, the dispersion of G^* is solely due to the establishment of network structures, i.e. at a state of a network with very few bonds, the viscoelastic behavior of the model is similar to what we found in agarose at low concentrations. Starting from such a plain gel sample, we sought to experimentally modify its internal structure (as measured by α) with minimal impact on its elastic properties (given by G'). The introduced method of embedding thin hydrophilic strips of a cigarette paper into the agar matrix caused the highest alteration of α (relative to G') in comparison to other composite materials tested in our lab. In our interpretation, the addition of paper yields an effective medium consisting of the cellulose of the paper strips and the sugar chains of the agarose matrix. Such a simple biphasic medium should be seen as a starting point for more elaborate structure modeling in elastography. While the resulting storage modulus of the effective medium is similar to that of the plain matrix, the loss modulus is considerably increased as an effect of the increased network density. Recent elastography studies using springpot-based multifrequency MRE reported α values of 0.251 (human healthy liver (Klatt *et al* 2010a)), 0.255 (brain, cortical region (Sack *et al* 2011)), 0.323 (brain, interior region (Sack *et al* 2011)), 0.292 (hydrocephalus brain, interior region (Streitberger *et al* 2011)), 0.253 (skeletal muscle, relaxed (Klatt *et al* 2010b)) and 0.270 (skeletal muscle, contracted (Klatt *et al* 2010b)). All these values were measured in 3D biomechanical systems of *in vivo* human organs. Consequently, comparison to α values determined by our 2D procedure is limited and we cannot assign *in vivo* α values to a specific fractal dimension of body tissue. In part II of this paper (Guo *et al* 2012), the tangled paper model is extended to three dimensions. Consistent with our model, Guo *et al* (2012) reported less effect of the fractal dimension on G^* since in a volume, network branches have a higher degree of freedom for avoiding intersection than in a 2D plane. Self-intersection or intersection with other branches is proportional to the number of cross-links and therewith to the network concentration p . Thus, we expected to observe a higher effect of D_f to viscoelasticity in 2D than in 3D since the alteration of p is larger in a plane than in a volume.

Further conclusions based on our paper-network model may not be applied to tissue in a straightforward manner. The entangled paper strips are not cross-linked, not multi-hierarchical and 2D. However, it is not the intention of this study to propose viscoelastic phantom materials as surrogate for natural fiber networks. This simple biphasic model is capable to experimentally support principle findings of 2D viscoelastic modeling. For further discussions we refer to part II of this study (Guo *et al* 2012).

In summary, a 2D finite lattice model of random scale-invariant network structure was proposed to study the viscoelastic behavior of soft biological tissues. The model was used to analyze the viscoelastic behavior of mechanical systems with self-similar geometries and relate the network topology to the mechanical properties of the effective medium. A link between network structure and viscoelastic properties was derived in terms of the powerlaw exponent of the complex shear modulus and the fractal network dimension. A high sensitivity of α to the fractal dimension was observed specifically in the range of $\alpha < 0.5$, which applies to *in vivo* biological tissue. Shear oscillatory rheometer experiments of agar gel samples confirmed the predicted increase in α resulting from the introduction of thin paper structures into a low-concentration agarose matrix. The proposed model may support the interpretation of dynamic elastography under various pathological and physiological conditions.

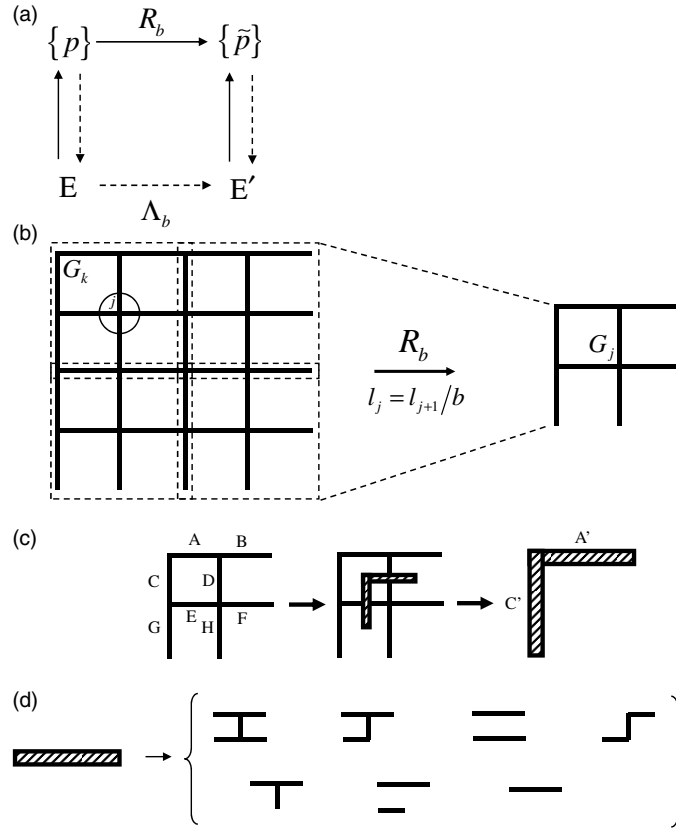


Figure A1. (a) Relation between renormalization Λ_b and probability transformation R_b . An ensemble E produces a set of $\{p\}$. E' is uniquely determined by $\{\tilde{p}\}$ only if the set $\{p\}$ inversely determines E (dashed vertical arrow). In this case, a renormalization Λ_b exists. (b) A block of lattice bonds for transformation with scale factor $b = 2$ and implicit change in scale length $l_j = l_{j+1}/b$. (c) The initial lattice is converted to another (rescaled self-dual) lattice. The connectedness of bond A' is thus determined by those of bonds $ABDEF$ as shown. The connectedness of bond C' is found from the original connectivity bonds $CDEGH$. (d) The renormalized element or super-bond includes the whole variety of possible configurations E of bonds with probability $\{p\}$ after transformation Λ_b . All these configurations are the same at all scales $l_j = l_{j+1}/b$.

Appendix

In this appendix, a generalized renormalization method according to Reynolds *et al* (1977) is described. In the first step we outline a block of bonds of size b for probability transformation $R_b: T^{b^d} \rightarrow T^2$ (figure A1(a)),

$$\tilde{p}_j = R_b([p_{k \in j}]). \quad (\text{A.1})$$

Straight brackets in equation (A.1) symbolize a group of bonds selected for transformation, while j is the level of hierarchy. After transformation R_b , a coarse-grained version of the lattice is obtained. The state of level j is characterized by bond probability \tilde{p}_j . Applying R_b to all levels j we may define the scale transformation which must fulfil the group property (Rotman 1994):

$$R_{b_1} R_{b_2} = R_{b_1 b_2}. \quad (\text{A.2})$$

In equation (A.2) indices 1 and 2 in b represent group elements of the transformation. For translationally invariant lattices, the group property in equation (A.2) is an approximation.

Let $\langle G^*(p) \rangle|_E$ be the ensemble average of $G^*(p)$, which depends on volume concentration p . We seek an ensemble E such that

$$\langle G^*(p) \rangle|_E = \beta \langle G^*(\tilde{p}) \rangle|_{E'}, \quad (\text{A.3})$$

where β is a nonlinear scaling parameter of averaged physical value after the transformation of the lattice. All statistical configurations generated by ensemble E should be the same as those given by transformed fractions of bonds \tilde{p} , which in turn are determined by E' . The relation

$$E' = \Lambda_b(E) \quad (\text{A.4})$$

defines the renormalization transformation Λ_b , assuming that E' exists (figure A1(a)). Since transformation R_b is not reversible after transformation Λ_b , we cannot obtain information about the distribution of G^* on scales smaller than b and thus we term R_b a semi-group.

This renormalization is illustrated in figure A1(b). In the left part of figure A1(b), we show a section of the original lattice while on the right we show the same section of the renormalized lattice.

A simple eight-bond unit with linear size $b = 2$ is chosen as a renormalization element (Bernasconi 1978). The process of coarsening is depicted in figure A1(c) with some more details. After transformation, the initial lattice is converted to another (rescaled self-dual) lattice, where each bond between two nearest neighboring sites of lower hierarchy represents a renormalization element. The connectedness of bond A' is thus determined by those of bonds ABDEF as shown in the middle part of figure A1(c). The connectedness of bond C' is found from the original connectivity bonds CDEGH. Recursive repetition of this operation results in a self-similar structure that hierarchically repeats the connectedness of the original bonds. If we consider only the horizontal or vertical spanning of the renormalization element, the connectivity in phase 1 will be determined only by five bonds (figure A1(d)). Given that each of these five bonds has a probability p or $q = 1 - p$ the resulting connectedness function $R_b(p)$ can be expressed by the polynomial equation

$$R_b(p) = p^5 + 5p^4(1-p) + 8p^3(1-p)^2 + 2p^2(1-p)^3, \quad (\text{A.5})$$

or after simplification

$$R_b(p) = 2p^5 - 5p^4 + 2p^3 + 2p^2. \quad (\text{A.6})$$

Equation (A.5) was constructed according to the following rules:

- The probability that a certain number of bonds with probability p and q is occupied is $p^5, p^4(1-p), p^3(1-p)^2$ and $p^2(1-p)^3$ (figure A1(d)).
- Only those configurations are considered which establish a connection between the left side and the right side of the cluster, thereby representing a single bond in the upper hierarchy level. The resulting numbers of possibilities are accounted for by the weighting factors 1, 5, 8, 2 limited by binomial coefficients.
- The connectedness function $R_b(p)$ is the weighted sum of probabilities of all possible bonds of phases 1 and 2.

According to point 2, an upper level hierarchy bond is established with probability

$$p_{j+1} = 2p_j^5 - 5p_j^4 + 2p_j^3 + 2p_j^2. \quad (\text{A.7})$$

The roots p_* of equation (A.7) in the physical meaningful range of $0 \leq p_* \leq 1$ are $p_* = \{0, 0.5, 1\}$. The first and third roots represent a fully cross-linked lattice and a homogeneous matrix without bonds, respectively. At these limits the system exhibits translational symmetry and stability in the parameter space. The second root $p_* = 0.5$ is unstable, i.e. a small perturbation in probability p leads to one of the stable homogeneous phases (Bernasconi 1978).

References

- Carcione J 2007 *Wave Fields in Real Media: Wave Propagation in Anisotropic, Anelastic, Porous and Electromagnetic Media* (Amsterdam: Elsevier)
- Clayton E H, Garbow J R and Bayly P V 2011 Frequency-dependent viscoelastic parameters of mouse brain tissue estimated by MR elastography *Phys. Med. Biol.* **56** 2391–406
- Deffieux T, Montaldo G, Tanter M and Fink M 2009 Shear wave spectroscopy for *in vivo* quantification of human soft tissues visco-elasticity *IEEE Trans. Med. Imaging* **28** 313–22
- Domb C and Lebowitz J L 2001 *Phase Transitions and Critical Phenomena* (London: Academic)
- Feller W 1968 *An Introduction to Probability Theory and Its Applications* (New York: Wiley)
- Geerligs M, Peters G W, Ackermans P A, Oomens C W and Baaijens F P 2008 Linear viscoelastic behavior of subcutaneous adipose tissue *Biorheology* **45** 677–88
- Gennisson J L, Deffieux T, Mace E, Montaldo G, Fink M and Tanter M 2010 Viscoelastic and anisotropic mechanical properties of *in vivo* muscle tissue assessed by supersonic shear imaging *Ultrasound Med. Biol.* **36** 789–801
- Guo J, Posnansky O, Hirsch S, Scheel M, Braun J and Sack I 2012 Fractal network dimension and viscoelastic powerlaw behavior: II. An experimental study of structure-mimicking phantoms by magnetic resonance elastography *Phys. Med. Biol.* **57** 4041
- Gurtovenko A A and Blumen A 2005 *Polymer Analysis, Polymer Theory* (Berlin: Springer) pp 171–282
- Hoyt K, Kneezel T, Castaneda B and Parker K J 2008 Quantitative sonoelastography for the *in vivo* assessment of skeletal muscle viscoelasticity *Phys. Med. Biol.* **53** 4063–80
- Jeong H, Tombor B, Albert R, Oltvai Z N and Barabasi A-L 2000 The large-scale organization of metabolic networks *Nature* **407** 651–4
- Klatt D, Friedrich C, Korth Y, Vogt R, Braun J and Sack I 2010a Viscoelastic properties of liver measured by oscillatory rheometry and multifrequency magnetic resonance elastography *Biorheology* **47** 133–41
- Klatt D, Hamhaber U, Asbach P, Braun J and Sack I 2007 Noninvasive assessment of the rheological behavior of human internal organs using multifrequency MR elastography: a study of brain and liver viscoelasticity *Phys. Med. Biol.* **52** 7281–94
- Klatt D, Papazoglou S, Braun J and Sack I 2010b Viscoelasticity-based Magnetic resonance elastography of skeletal muscle *Phys. Med. Biol.* **55** 6445–59
- Landau L D, Lifshitz E M and Pitaevskii L P 1980 *Statistical Physics* (Amsterdam: Elsevier)
- Magin R L and Royston T J 2010 Fractional-order elastic models of cartilage: a multi-scale approach *Commun. Nonlinear Sci. Numer. Simul.* **15** 657–64
- Mandelbrot B B 1983 *The Fractal Geometry of Nature* (New York: Freeman)
- Milton G M 2002 *Theory of Composites* (Cambridge: Cambridge University Press)
- Muthupillai R and Ehman R L 1996 Magnetic resonance elastography *Nature Med.* **2** 601–3
- Ophir J, Céspedes I, Ponnekanti H, Yazdi Y and Li X 1991 Elastography: a quantitative method for imaging the elasticity of biological tissues *Ultrason. Imaging* **13** 111–34
- Papazoglou S, Hirsch S, Braun J and Sack I 2012 Multifrequency inversion in magnetic resonance elastography *Phys. Med. Biol.* **57** 2329–46
- Parker K J, Huang S R, Musulin R A and Lerner R M 1990 Tissue response to mechanical vibrations for ‘sonoelasticity imaging’ *Ultrasound Med. Biol.* **16** 241–6
- Plewes D B, Betty I, Urchuk S N and Soutar I 1995 Visualizing tissue compliance with MR imaging *J. Magn. Reson. Imaging* **5** 733–8
- Reynolds P J, Klein W and Stanley H E 1977 A real-space renormalization group for site and bond percolation *J. Phys. C: Solid State Phys.* **10** L167–72
- Riek K, Klatt D, Nuzha H, Mueller S, Neumann U, Sack I and Braun J 2011 Wide-range dynamic magnetic resonance elastography *J. Biomech.* **44** 1380–6
- Sack I, Streitberger K J, Krefting D, Paul F and Braun J 2011 The influence of physiological aging and atrophy on brain viscoelastic properties in humans *Plos One* **6** e23451
- Schiessel H and Blumen A 1995 Mesoscopic pictures of the sol–gel transition—ladder models and fractal networks *Macromolecules* **28** 4013–9
- Sinkus R, Siegmann K, Xydeas T, Tanter M, Claussen C and Fink M 2007 MR elastography of breast lesions: understanding the solid/liquid duality can improve the specificity of contrast-enhanced MR mammography *Magn. Reson. Med.* **58** 1135–44
- Stanley H E 1978 *Introductions to Phase Transitions and Critical Phenomena* (Oxford: Oxford University Press)
- Streitberger K J *et al* 2011 *In vivo* viscoelastic properties of the brain in normal pressure hydrocephalus *NMR Biomed.* **24** 385–92
- Vappou J, Breton E, Choquet P, Goetz C, Willinger R and Constantinesco A 2007 Magnetic resonance elastography compared with rotational rheometry for *in vitro* brain tissue viscoelasticity measurement *Magma* **20** 273–8

- Xu H, Rao M, Varghese T, Sommer A, Baker S, Hall T J, Sisney G A and Burnside E S 2010 Axial-shear strain imaging for differentiating benign and malignant breast masses *Ultrasound Med. Biol.* **36** 1813–24
- Yin M, Talwalkar J A, Glaser K J, Manduca A, Grimm R C, Rossman P J, Fidler J L and Ehman R L 2007 Assessment of hepatic fibrosis with magnetic resonance elastography *Clin. Gastroenterol. Hepatol.* **5** 1207–13
- Zhang M, Nigwekar P, Castaneda B, Hoyt K, Joseph J V, di Sant'Agnese A, Messing E M, Strang J G, Rubens D J and Parker K J 2008 Quantitative characterization of viscoelastic properties of human prostate correlated with histology *Ultrasound Med. Biol.* **34** 1033–42
- Ziol M *et al* 2005 Noninvasive assessment of liver fibrosis by measurement of stiffness in patients with chronic hepatitis C *Hepatology* **41** 48–54